atmosphere

MDPI

Article

Investigating the Temporal and Spatial Characteristics of Lower Atmospheric Ducts in the Arctic via Long-Term Numerical Simulations

Jinyue Wang [1], Xiaofeng Zhao [2], Jing Zou [1,*], Pinglv Yang [2], Bo Wang [1], Shuai Yang [1], Zhijin Qiu [1], Zhiqian Li [1], Tong Hu [1] and Miaomiao Song [1]

[1] Institute of Oceanographic Instrumentation, Qilu University of Technology (Shandong Academy of Sciences), Qingdao 266001, China; 10431220646@qlu.edu.cn (J.W.); wangbo0532@qlu.edu.cn (B.W.); 10431220708@stu.qlu.edu.cn (S.Y.); qzj@qlu.edu.cn (Z.Q.); lizhiqian@qlu.edu.cn (Z.L.); tong.hu@qlu.edu.cn (T.H.); mmsong@qlu.edu.cn (M.S.)

[2] College of Meteorology and Oceanography, National University of Defense Technology, Changsha 410003, China; zhaoxiaofeng@nudt.edu.cn (X.Z.); ypl@nudt.edu.cn (P.Y.)

* Correspondence: zoujing@qlu.edu.cn

Abstract: In this study, a diagnostic model for lower atmospheric ducts was developed using the polar weather research and forecasting model. A five-year simulation was then conducted across the entire Arctic region to investigate the temporal and spatial characteristics of lower atmospheric ducts. The model demonstrated excellent performance in simulating modified atmospheric refractivity, with root mean square errors ranging from 0 M to 5 M. The five-year simulation results revealed that duct occurrence rates across the Arctic region were all below 1% and exhibited a negative relationship with latitude. Regarding the difference between surface ducts and elevated ducts, a higher frequency of surface ducts was detected in the Arctic region. The height and thickness of surface ducts were generally lower than those of elevated ducts, but the strength of surface ducts was slightly greater. Regionally, surface ducts mainly occurred in the land areas surrounding the Arctic Ocean, while more elevated ducts were found in the North Atlantic Sea area. Additionally, a negative correlation was observed between the polar vortex indices and the characteristics of ducts, particularly for surface ducts. The ducts in Greenland were notably influenced by polar vortex activity, whereas the ducts in other regions, such as the Norwegian Sea and Kara Sea, were less affected.

Keywords: lower atmospheric duct; spatio-temporal characteristic; climatic simulation; seasonal variation; Arctic Sea

Academic Editors: Stergios Kartsios, Ioannis Pytharoulis and Flavio T. Couto

Received: 7 November 2024
Revised: 12 December 2024
Accepted: 23 December 2024
Published: 26 December 2024

Citation: Wang, J.; Zhao, X.; Zou, J.; Yang, P.; Wang, B.; Yang, S.; Qiu, Z.; Li, Z.; Hu, T.; Song, M. Investigating the Temporal and Spatial Characteristics of Lower Atmospheric Ducts in the Arctic via Long-Term Numerical Simulations. *Atmosphere* **2025**, *16*, 11. https://doi.org/10.3390/atmos16010011

1. Introduction

Atmospheric duct is a phenomenon characterized by abnormal electromagnetic wave propagation, typically caused by the uneven vertical distributions of the atmospheric refractivity. This special weather phenomenon can induce a significant impact on the propagation of electromagnetic waves [1]. During this phenomenon, electromagnetic waves become trapped at specific altitudes due to excessive bending of their trajectories. This trapping significantly impacts the performance of radio equipment [2,3]. For example, atmospheric ducts can cause local mobile base stations to receive signals from beyond their normal communication range. These additional signals often lead to same-frequency interferences during local signal transmission and reception, resulting in communication delays or interruptions [4]. Atmospheric ducts can also enable over-the-horizon detection

of radar signals while creating blind detection zones at certain altitudes, which significantly impacts radar target detection [5–7]. Within the trapping layer formed by the ducts, the path loss of radio wave propagation is substantially reduced [8,9]. Consequently, the effective range of radar and microwave signal transmitters increases [10]. For example, in April 2022, a coastal radar in Odessa, Ukraine, detected a target at more than twice its standard effective detection range, which led to the launch of two anti-ship missiles, which struck and ultimately sank the Russian ship "Moskva". Norin et al. [11] analyzed the weather conditions during the event and simulated the radar wave propagation process. Their findings revealed the presence of a strong atmospheric duct occurred in the Black Sea area. In such a ducting environment, ground radar signals could detect targets at greater distances with reduced losses. This study theoretically confirmed the feasibility of beyond-visual-range missile strikes. In the marine environment, the isotropic nature of the sea surface makes atmospheric ducting more frequent. Therefore, a thorough understanding of the temporal and spatial variations of marine atmosphere can have practical applications in various fields, including ship navigation, communication planning, radar design, and more [12].

Lower atmospheric ducts are typically defined as those occurring in the lower and middle troposphere, generally at altitudes below 500 hPa or 5000 m. Atmospheric ducting can occur in regions across nearly all latitudes, provided specific conditions are met. These ducts are mainly caused by abnormal vertical variations in atmospheric refractivity, which are influenced by the distribution of temperature and humidity [13]. Bean et al. [14] developed an empirical model to calculate the atmospheric refractivity index (N) using air temperature, pressure, and water vapor pressure. Their study identified temperature inversions and sharp decreases in humidity as the key weather conditions contributing to the formation of atmospheric ducts. The inversion phenomenon does not necessarily result in the formation of atmospheric ducts, but atmospheric ducts are often accompanied by inversion layers. The vertical gradient of air temperature is a critical factor influencing the gradient of the atmospheric refractive index. In the Arctic region, temperature inversions contribute to the frequent occurrence of atmospheric ducts. Inversion layers are typically associated with abrupt changes in the atmospheric refractive index gradient, which facilitate and enhance the formation of atmospheric ducts to some extent. These inversions usually occur near the surface and promote the development of surface ducts. This is the primary reason why surface ducts are significantly more common than elevated ducts. The intensity of surface ducts is directly influenced by the thickness and strength of the inversion layer. Consequently, the presence of an inversion not only increases the likelihood of duct formation but also enhances the properties of existing ducts. Inversions occurring at higher altitudes can facilitate the formation of elevated ducts. These elevated ducts typically form above the inversion layer and enable the transmission of radio waves without interference from the complex terrain of the earth. While high-altitude inversion phenomena are less common in the Arctic, when they do occur, they tend to be extensive and intense, leading to large-scale elevated duct phenomena. This relationship is represented by the following empirical model:

$$N = \frac{77.6}{T}\left(P + 4810\frac{e}{T}\right), \tag{1}$$

where N denotes the atmospheric refractivity index (N—units), T denotes the atmospheric temperature (K), P denotes the atmospheric pressure (hPa), and e denotes the water vapor pressure (hPa). The water vapor pressure e can be calculated using the following equation [15]:

$$e = \frac{qP}{\varepsilon + (1-\varepsilon)q}, \tag{2}$$

where q is the specific humidity (g/kg) and ε is a constant (usually 0.622).

The atmospheric refractivity index can be adjusted to the modified atmospheric refractivity index by accounting for the curvature effects of the earth at different altitudes:

$$M = N + \frac{h}{R_e} \times 10^6 = N + 0.157h, \quad (3)$$

where M is the modified atmospheric refractivity index (M—unit); R_e is the radius of the earth (6371 km); and h is height (m). The characteristics of lower atmospheric ducts can be analyzed based on the vertical gradient distribution of the modified atmospheric refractivity.

Numerous studies have explored the spatial and temporal characteristics of the lower atmospheric ducts in various seas worldwide using numerical simulations. For example, Zhu et al. [16] employed the fifth-generation Pennsylvania State University National Center for Atmospheric Research Mesoscale Model (MM5) to simulate the lower atmospheric ducts in the Persian Gulf region. Their findings revealed that the simple surface ducts, surface ducts with base heights, and elevated ducts were all distributed from northwest to southeast. The spatial patterns of these ducts were influenced by sea–land wind circulation and changes in the atmospheric boundary layer. Similarly, Atkinson et al. [17] developed a duct prediction model using MM5. The evaluation in the Persian Gulf region showed that the simulated atmospheric duct characteristics closely matched the observed data. Burk et al. [18] used the U.S. Navy Operational Regional Atmospheric Prediction System (NORAPS) to simulate the weather conditions associated with atmospheric ducts in the coastal regions of the Southern California Bight. They found that sea−land wind circulation altered the structure of the atmospheric boundary layer, often resulting in the formation of more stratocumulus clouds at the top of the boundary layer. These changes also led to more significant diurnal variations of atmospheric ducts in the region. Haack and Burk [19] employed the Coupled Ocean–Atmosphere Mesoscale Prediction System (COAMPS) to simulate the mechanisms of atmospheric duct formation off the coast of California. They discovered that as the height of the atmospheric boundary layer decreased, surface ducts were strengthened, typically accompanied by a weaker elevated duct above.

However, most previous studies have focused on duct characteristics in low- and mid-latitude regions, with relatively few studies on lower atmospheric duct modeling in high-latitude seas, where human activity is limited. The Arctic region, predominantly covered by the Arctic Ocean, is mainly composed of sea ice and glaciers. It experiences a cold climate, with much of its surface frozen year-round, violent storms during the cold season, and sea spray in the warmer months. As global greenhouse gas concentrations rise, the Arctic climate is changing rapidly. The temperature in the Arctic has been observed to increase at twice the rate of the global average [20], and sea ice in Arctic waters is melting at an accelerated pace, with multi-year sea ice cover now reduced to less than one-third of its previous extent [21]. These changes in the meteorological and hydrological environment are expected to impact the characteristics of lower atmospheric duct phenomena.

In the few studies on Arctic atmospheric duct characteristics, researchers have typically relied on single-station observations or reanalysis datasets for duct diagnosis and analysis. For example, Qin et al. [22] used the ERA–Interim reanalysis data from the European Centre for Medium-Range Weather Forecasts (ECMWF) to analyze the climatic characteristics and variations of atmospheric ducts in the Arctic from 1989 to 2018. Their findings revealed that the overall frequency of atmospheric ducts in the Arctic was relatively low, with surface ducts occurring two to three times more frequently than elevated ducts. Zhu et al. [23] analyzed the characteristics of atmospheric ducts in the Svalbard Islands in the Arctic using reanalysis data. They found that the surface duct occurrence rate was 12.6%, with an average intensity of 1.30 M and an average thickness of 13 m.

The characteristics of atmospheric ducts are derived from diagnostic information on the vertical distribution of atmospheric refractivity anomalies. For reanalysis data with lower resolution and fewer vertical layers, the refractivity profiles tend to be relatively smooth. While the mean error between these profiles and sounding data is not large, the diagnostic atmospheric duct information based on these profiles may differ significantly from the sounding data. In previous studies, we compared model simulation results with direct diagnostics from reanalysis data and found that atmospheric duct information from numerical models was more accurate [24,25]. Therefore, to better simulate and analyze Arctic atmospheric ducts, this study uses a numerical model driven by reanalysis data to conduct dynamic downscaling simulations.

The Polar Weather Research and Forecasting (PWRF) model was developed for polar weather simulations by the Polar Meteorology Group at the Byrd Polar and Climate Research Centre, Ohio State University. The PWRF model builds on the original weather research and forecasting (WRF) model and incorporates considerations for sea ice surfaces and corresponding parameterization modifications. PWRF is widely used in polar research. For example, Hines et al. [26] applied this model in simulations of the western Arctic and found that the results matched well with near-surface observations. The correlation coefficients between the sounding observations and simulated air pressure, temperature, and wind speed typically exceeded 0.7. Similarly, Deb et al. [27] also used the PWRF model to simulate the weather processes in West Antarctica and found that the model performed well in simulating surface air pressure, with correlation coefficients greater than 0.97. The model also demonstrated better performance in simulating inland wind speeds compared with coastal regions. Additionally, Wilson et al. [28] found that the tropospheric temperatures simulated by the PWRF model, with deviations typically less than 1 °C, generally agreed with ERA-Interim reanalysis data. In this study, the PWRF model will be used to develop a diagnostic scheme for lower atmospheric ducts. We conducted a five-year continuous simulation for the entire Arctic region. The goal of this study is to analyze the spatial and temporal variability of lower atmospheric ducts through long-term dynamic downscaling simulations.

Studying the spatio-temporal characteristics and long-term variation patterns of atmospheric ducts in the Arctic region provides valuable insights for the design and deployment of communication and radar systems in this area. The presence and changes in atmospheric ducts can significantly impact the propagation range, stability, and quality of electromagnetic signals. Particularly in the unique environment of the polar regions, the duct effect can lead to complex propagation conditions. Therefore, when designing and deploying communication and radar systems, it is essential to consider the long-term variation patterns of local atmospheric ducts. This will help optimize system parameters such as frequency selection, signal transmission power, antenna design, and deployment location and consequently improve signal coverage, communication stability, and surveillance capabilities. Furthermore, our study explores the relationships between atmospheric elements, polar vortex indices, and atmospheric ducts. This research can help researchers understand the formation and variation patterns of polar atmospheric ducts, provide valuable meteorological data to support the design of various radio systems, and ensure their efficient and reliable operation in the harsh polar environment.

The second section of this paper provides a description of the model, the duct diagnostic process, and the validation data used. The third section presents the experimental design and model configuration of the PWRF, based on the results of the previous sensitivity tests. In the fourth section, we will briefly evaluate the simulation results and then analyze the spatial and temporal characteristics of the lower atmospheric ducts. Finally, in the fifth section presents the conclusion and discusses the uncertainties in the results.

2. Model and Data Description

2.1. Polar WRF Model

The WRF model is one of the most commonly used weather simulation tools. However, it has relatively large errors when simulating polar weather. To address this, the Polar WRF (PWRF) model was developed as a polar version of the WRF model [29]. Compared with the standard WRF model, PWRF includes a sea ice scheme in the land surface model. The parameters for calculating sea ice thickness and snow depth in this scheme are adjusted dynamically. As a result, the sea-ice albedo and snow water equivalent on sea ice are no longer fixed but vary with seasonal changes. Additionally, the snow thermal processes and surface heat flux processes of the model were modified to better suit the environmental characteristics of the polar regions [30,31]. PWRF has proven to be an excellent tool and is widely used for polar weather modeling.

In this study, the Polar WRF model is used to simulate meteorological processes in Arctic regions and allows for a more accurate representation of the unique environmental conditions in the Arctic. The following are several aspects that address these polar-specific conditions: The geographical features of the Arctic region are highly distinctive, with vast oceans, ice-covered land, and the seasonal alternation of day and night. Traditional meteorological models are often unsuitable for this polar environment. However, the Polar WRF model can better predict characteristics such as ice surface albedo, heat flux, and atmospheric stability. This model is capable of simulating long-term climate data and capturing the long-term impacts of polar seasonality and day–night variations on the atmosphere, including seasonal fluctuations in air temperature, wind speed, and humidity. The model can also accurately simulate atmospheric stability in cold regions, including the formation of the inversion layer, humidity distribution, and heat exchange. Additionally, cloud and precipitation systems in the Arctic typically contain higher concentrations of ice crystals and aerosols. The PWRF simulates these characteristics using a specialized cloud microphysics process module, which accurately calculates cloud formation, precipitation patterns, and the interaction between cold and warm air masses. In the simulation of the lower atmosphere, the polar WRF features a unique design for the generation of the inversion layer, which allows it to precisely simulate the thickness, intensity, and duration of the inversion layer. Additionally, the model accounts for factors such as radiative cooling and heat transfer, which influence the behavior of the inversion layer.

2.2. Diagnosis Scheme of Lower Atmospheric Ducts

Previous studies have shown some disagreement regarding the classification of lower atmospheric ducts. Some studies classified the ducts into three types based on their formation mechanisms and spatial distribution: evaporation ducts, surface ducts with base heights, and elevated ducts [32]. Other studies proposed a four-type classification, including simple surface ducts, S-type surface ducts with base heights, elevated ducts and composite ducts [33]. The primary disagreement lies in the distinction between evaporation ducts and composite ducts.

In this study, we considered the classifications from both types of studies and classified the lower atmospheric ducts into five categories based on the refractivity profile characteristics (as shown in Figure 1). These categories include evaporation ducts, simple surface ducts, S-type surface ducts with base heights, elevated ducts, and composite ducts. Among them, the height of evaporation ducts typically ranges from 1 to 40 m [34]. Owing to the difficulty in accurately simulating these ducts with numerical models, researchers typically rely on empirical formulas for their simulations. Therefore, this study does not focus on evaporation ducts but instead concentrates on diagnosing the characteristics of the other lower atmospheric ducts.

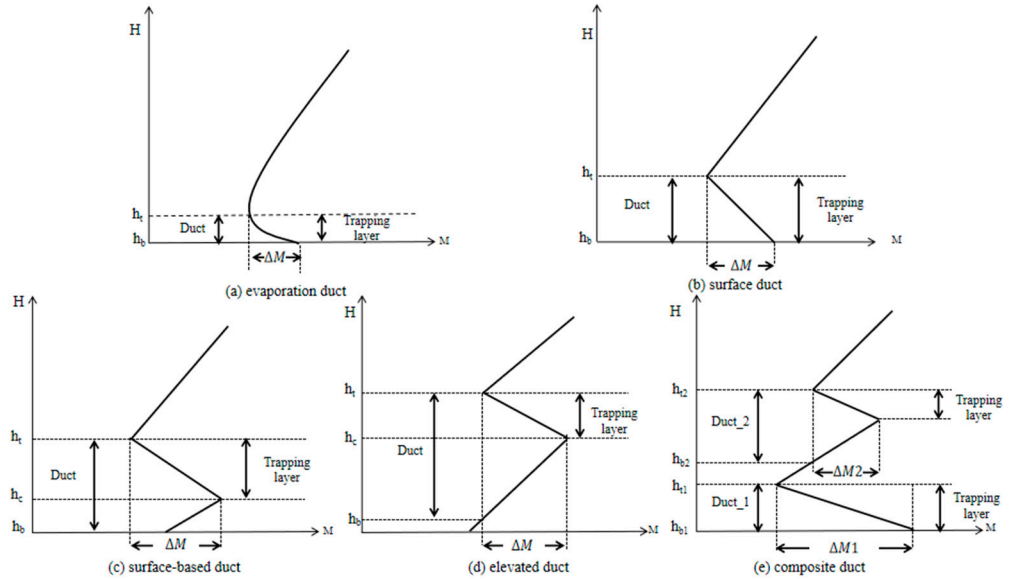

Figure 1. Typical modified refractivity profiles of lower atmospheric duct types distinguished in this study include (**a**) evaporation ducts, (**b**) surface ducts, (**c**) surface-based ducts, (**d**) elevated ducts, and (**e**) composite ducts; h_t is trapping layer top height, h_c is trapping layer bottom height, and h_b is duct bottom height.

Figure 2 illustrates the flowchart of the lower atmospheric duct diagnostic module developed in this study based on the outputs of PWRF. The process mainly involves the following steps:

(a) Read the air temperature, humidity, altitude, and pressure outputs from PWRF. Then, calculate the modified atmospheric refractivity index (M) using Equations (1)–(3). Set the initial altitude to $h_0 = 0$ and check for the occurrence of a duct, which starts from the lowest layer.

(b) Starting from the initial height h_0, look upwards to identify the first point of maximum modified atmospheric refractivity $M(h)$. If no maximum values are found, there is no duct layer, and the diagnosis ends; if maximum values are found, continue the diagnostic process.

(c) Check whether the diagnosed duct intensity exceeds the set threshold. If it does, label it as the first-layer duct; otherwise, classify it as atmospheric disturbance.

(d) If the first-layer duct exists, determine whether the modified atmospheric refractivity at the top of the duct is less than or equal to the refractivity of the lowest layer. If so, classify it as a surface duct; otherwise, label it as an elevated duct.

(e) For a surface duct, determine whether the modified atmospheric refractivity at the base of the duct is greater than the refractivity at the lowest height. If so, the duct is classified as a surface duct with a base height; otherwise, it is considered a simple surface duct near the sea surface.

(f) Calculate the average height of the duct, which is the mean of the top and bottom heights of the duct. The duct thickness is the difference in height between the top and bottom of the duct.

(g) Determine whether the current h_t is the maximum height; if not, return to step (c) and continue searching at a higher altitude. If it is the maximum height, proceed with the diagnosis.

(h) Check whether the duct consists of more than one layer. If not, the current duct is a single-layer duct. If it has multiple layers, it is classified as a composite duct.

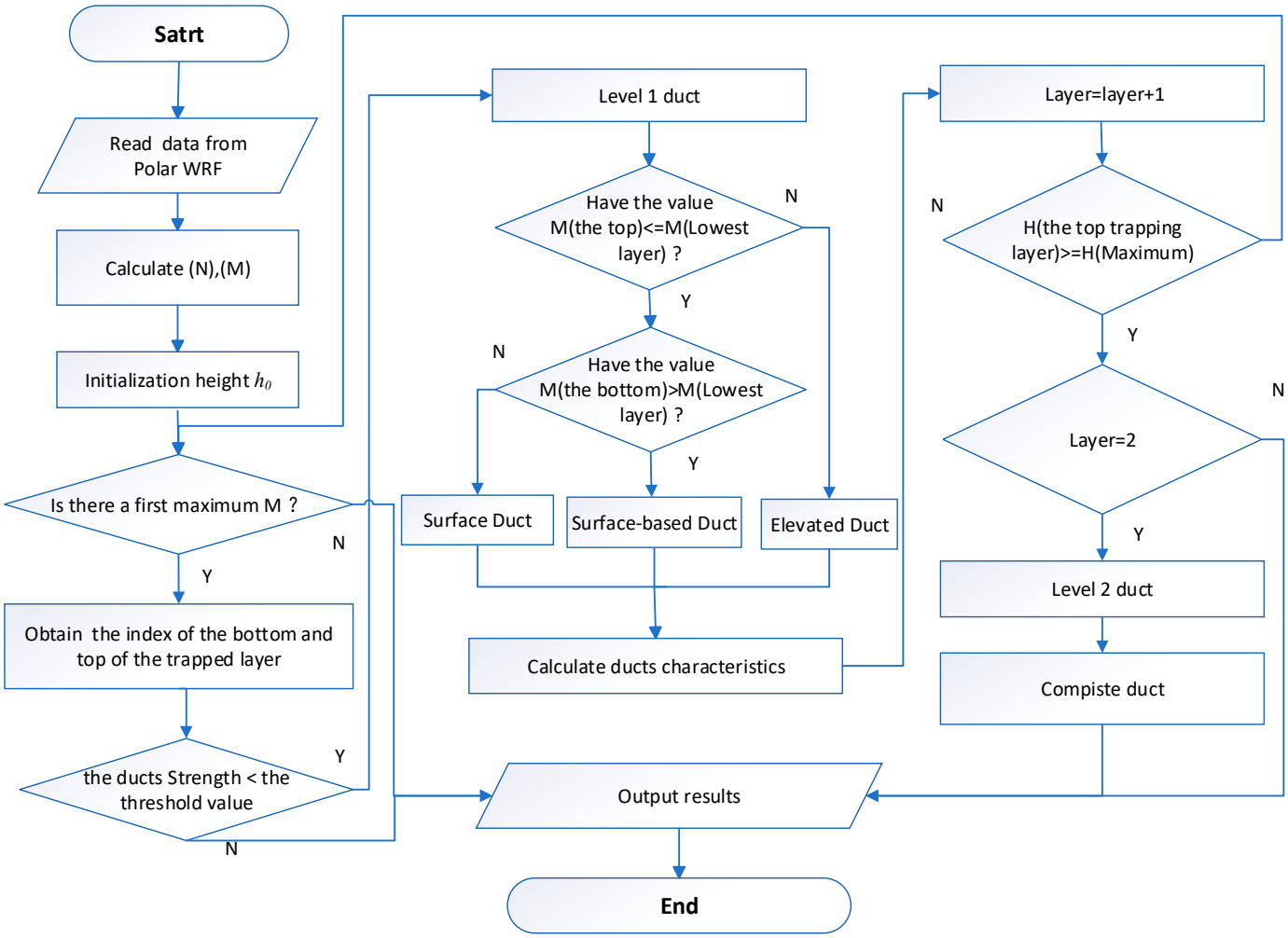

Figure 2. Flowchart of the lower atmospheric duct diagnosis module developed in this study.

2.3. Diagnosis Scheme of Polar Vortex Ducts

The polar vortex is a large-scale cold vortex system and a crucial component of the atmospheric circulation in the polar regions. It is a cyclone system characterized by the rotation of cold air at high altitudes. In the Arctic, the polar vortex mainly resides in the middle of the troposphere and extends into the stratosphere. It plays a significant role in influencing weather patterns in the region. In this study, we explored the relationship between the polar vortex and atmospheric duct characteristics by calculating the intensity and area index of the polar vortex.

The calculation of polar vortex indices varied slightly among previous studies. The indices were mainly derived by diagnosing the geopotential height at 500 hPa, a level where the intensity and shape of the polar vortex are known to be more stable. For example, Burnett [35], Davis and Benkovic [36], and Markham [37] all used geopotential heights at 500 hPa to investigate the variability of the polar vortex. This study also adopted their diagnostic approach.

2.3.1. Calculation of Polar Vortex Intensity

The monthly mean Polar Vortex Intensity (PVI) index was calculated using the method proposed by Erik W. Kolstad [38]:

$$\mathrm{PVI} = \frac{\sum(Z' \cos \varphi)}{\sum \cos \varphi}, \tag{4}$$

Here, $Z' = Z - \overline{Z}$, and Z is the geopotential height at 500 hPa, $\overline{Z}$ is the climatological state mean, and φ is the latitude. All grid points across the entire Arctic region were included in the calculation process.

2.3.2. Calculation of Polar Vortex Area

Albert Peterlin et al. [39] calculated the area enclosed by the 500 hPa geopotential height and defined this area as the polar vortex area (PVA) index. This study adopted the same method to calculate the PVA index, using the following equation:

$$\mathrm{PVA} = \int_{\varphi}^{\frac{\pi}{2}} \int_{\lambda_1}^{\lambda_2} {R_e}^2 \cos\varphi \mathrm{d}\varphi \mathrm{d}\lambda = {R_e}^2 (1 - \sin\varphi)(\lambda_2 - \lambda_1), \quad (5)$$

where R_e is the radius of the Earth, φ is the latitude of the polar vortex boundary, and λ is the longitude of the enclosed area.

2.4. Observation Data for Evaluation

The simulation results were validated using sounding data from three representative radiosonde stations: Ostrov Dikson (ID 20674, Russia), Barrow (ID 70026, United States), and Danmarkshavn (ID 04320, Greenland). The data was sourced from the University of Wyoming's website (http://weather.uwyo.edu/ (accessed on 1 April 2024)). The observed meteorological elements were recorded twice a day (00 h UTC and 12 h UTC) and included air pressure, geopotential height, temperature, dew point temperature, relative humidity, and other relevant parameters.

Additionally, the ECMWF Reanalysis v5 (ERA5) data [40], the fifth generation of atmospheric reanalysis data produced by the ECMWF, was also included in this study as a reference. This dataset is accessible at https://www.ecmwf.int/en/forecasts/dataset/ecmwf-reanalysis-v5 (accessed on 5 November 2023). The ERA5 dataset was generated using the general circulation model, which integrates observational data from various sources, such as ground stations and satellites. It has been widely utilized as reference data for model evaluation and mechanism analysis. The dataset features a spatial resolution of 0.25° × 0.25°, a vertical resolution of 37 layers ranging from 1000 hPa to 1 hPa, and a temporal resolution of one h.

3. Experimental Design

In this study, the area north of 60° N was selected as the study region. Figure 3 shows the topographic height map within the PWRF simulation, with yellow dots marking the locations of the three sounding stations used for model validation.

The model grids had dimensions of 2644 × 202, with a horizontal resolution of approximately 15 km and 51 vertical layers. According to previous sensitivity tests, the parameterization schemes used in PWRF were as follows: the WRF Single Moment 6 class (WSM6) scheme [41] for cloud microphysics, the MM5 scheme [42] for the surface layer process, the Yonsei University (YSU) scheme [43] for the boundary layer process, the Rapid Radiative Transfer Model (RRTM) longwave radiation scheme [44], the Dudhia scheme [45] for shortwave radiation, and the Grell–Freitas scheme [46] for cumulus cloud parameterization. The grid nudging method [47] was applied for boundary field processing in PWRF. This method involved a grid-to-grid relaxation forcing term to approximate the analytical field. Essentially, it was a four-dimensional assimilation technique that periodically integrated regional and boundary information from the driving field to constrain the simulation results, thereby enhancing simulation accuracy.

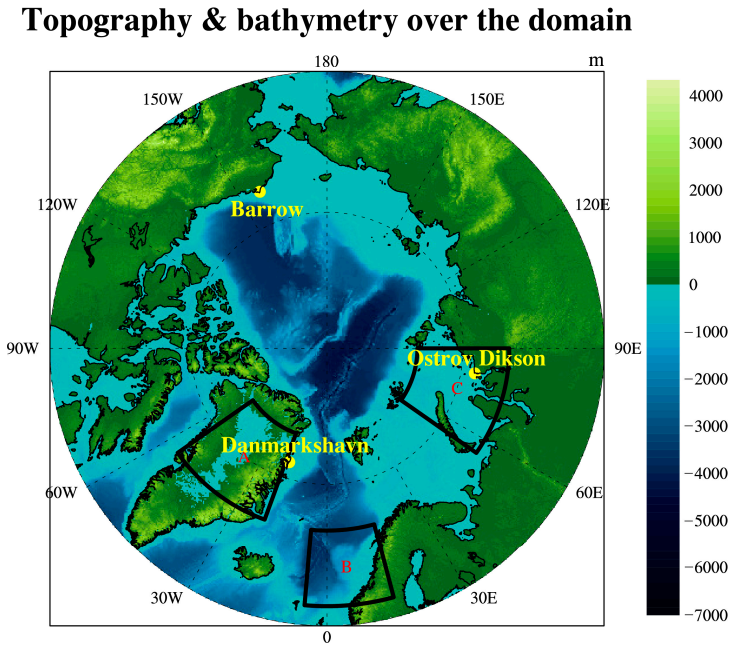

Figure 3. Topographic map of the domain used in the polar WRF model for this study. The locations of the three sounding stations for validation are marked with yellow dots. The three areas framed by black lines represent the typical regions selected for the subsequent statistical analysis, where A represents Greenland, B represents the Norwegian Sea, and C represents the Kara Sea.

The driving dataset used was the ERA5 reanalysis data. The long-term simulation ran from 00:00 UTC on 31 December 2016 to 00:00 UTC on 1 January 2022, which covered a total of five years. As PWRF is a mesoscale weather model, continuous integration over such a long period can lead to error accumulation. Previous studies have shown that dividing long-term continuous integration into shorter segments effectively reduces error growth in extended simulations [48]. Therefore, based on prior sensitivity analyses, this study employed a segmented integration approach for the long-term simulations. The PWRF model was run for six days at a time, with the results from the first day used for spin-up and the following five days used for analysis. The atmospheric duct phenomena were isolated extreme events, which differed from continuously varying variables such as temperature and humidity; hence, this segmented approach did not affect the statistical analysis of atmospheric duct characteristics.

4. Results

4.1. Error Evaluation of the Historical Simulations at Radiosonde Stations

The error evaluation was conducted using data from three radiosonde stations—Ostrov Dikson, Barrow, and Danmarkshavn—covering the year 2017. Figure 4 presents the vertical profiles of statistical indices of modified atmospheric refractivity, with the interpolated ERA5 reanalysis data shown for comparison. The statistical indices included the mean error (*ME*), correlation coefficient (*CC*), and root mean square error (*RMSE*). The formulas for these indices are as follows:

$$ME = \frac{\sum_{i=1}^{n}(y_i - x_i)}{n}, \tag{6}$$

$$CC = \frac{\sum_{i=1}^{n}(x_i - \overline{x})(y_i - \overline{y})}{\sqrt{\sum_{i=1}^{n}(x_i - \overline{x})^2 (y_i - \overline{y})^2}}, \tag{7}$$

$$RMSE = \sqrt{\frac{\sum_{i=1}^{n}(x_i - y_i)^2}{n}}, \tag{8}$$

where $\overline{x} = \frac{\sum_{i=1}^{n} x_i}{n}$, $\overline{y} = \frac{\sum_{i=1}^{n} y_i}{n}$, i represents the i-th data point, used to identify specific observed and simulated data, and n represents the total number of data points. x_i is the observed data, and y_i is the simulated data.

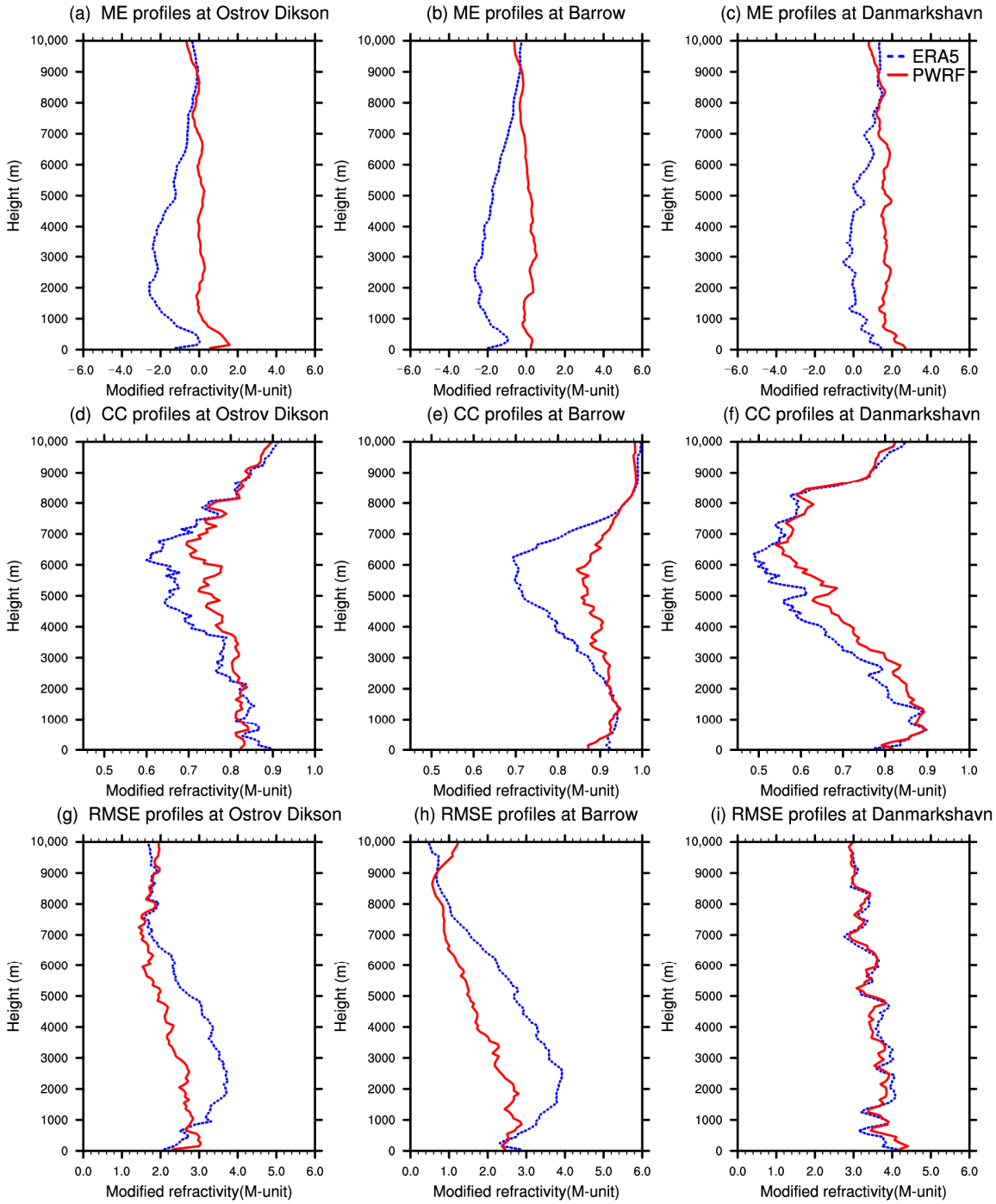

Figure 4. Mean error (ME) profiles of the modified atmospheric refractivity at (**a**) Ostrov Dikson, (**b**) Barrow and (**c**) Danmarkshavn radiosonde stations; the mean correlation coefficient (CC) profiles of the modified atmospheric refractivity at (**d**) Ostrov Dikson, (**e**) Barrow, and (**f**) Danmarkshavn radiosonde stations; and the root-mean-square error (RMSE) profiles of the modified atmospheric refractivity at (**g**) Ostrov Dikson, (**h**) Barrow, and (**i**) Danmarkshavn radiosonde stations. The red lines represent the PWRF results, and the blue dashed lines represent the ERA5 reanalysis data.

Figure 4a–c display the profiles of the MEs for the modified atmospheric refractivity at the three stations. As shown in the figure, the MEs for both PWRF and ERA5 ranged from −4 M to 4 M and exhibited similar trends. An extreme error was observed below 3000 m for both the simulation and ERA5 data. Above 3000 m, the errors gradually decreased with increasing height. Compared with the ERA5 reanalysis data, the PWRF simulations exhibited lower MEs, with mean values of 0.04 M, −0.06 M, and 1.56 M at the three stations, respectively. In contrast, the MEs for the ERA5 data were −1.18 M, −1.46 M, and 0.59 M. Figure 4d–f show the profiles of the CCs. Overall, the correlation between the simulation and observation decreased with increasing height and then increased again. A minimum value occurred between 5000 m and 7000 m, which was also the height range where the difference between the PWRF and ERA5 data was largest. On average, the CCs between PWRF and the observations were 0.79, 0.92, and 0.73 at the three stations. The CCs for ERA5 were slightly lower, with values of 0.77, 0.87, and 0.69. Figure 4g–i show the profiles of the RMSEs. The RMSE values ranged from 0 M to 4 M within the height range of 10,000 m. PWRF had lower RMSE values of 2.17 M, 1.68 M, and 3.46 M, while the ERA5 data exhibited higher RMSE values of 2.58 M, 2.33 M, and 3.48 M, respectively.

Overall, the modified atmospheric refractivity simulated by PWRF performed slightly better than the ERA5 reanalysis data at all three radiosonde stations. The errors in the PWRF simulations remained stable up to a height of 10,000 m, which demonstrated high accuracy. This stability made PWRF well-suited for the subsequent atmospheric duct diagnosis.

4.2. Spatial Distributions of the Lower Atmospheric Duct Characteristics

According to the duct diagnostics from the five-year simulation, the characteristics of Arctic lower atmospheric ducts were statistically analyzed. Figure 5 shows the multi-year mean spatial distributions of the occurrence rates for the four types of lower ducts defined in Section 2.2. In Figure 5a, the average occurrence rate of simple surface ducts across the entire region was 0.23%. Simple surface ducts were characterized by the modified atmospheric refractivity at the duct top being lower than at ground level. These ducts featured a duct layer that directly included a grounded trapping layer. As shown in Figure 5a, this type of duct mainly occurred in land areas surrounding the Arctic Ocean. The formation of simple surface ducts was likely driven by the development of cold high-pressure systems and local radiative cooling, which created temperature inversions. In terms of regional distribution, the occurrence rate of simple surface ducts was higher on land than over the oceans, and the rates were greater at lower latitudes compared with higher latitudes. The occurrence of atmospheric ducts was influenced by factors such as air temperature, humidity, sea surface temperature (SST), and air pressure. When changes in air pressure were minimal, variations in air temperature and humidity became the main factors determining the occurrence of atmospheric ducts. Many previous studies have found that the incidence rate of surface ducts over land was higher than that over the sea. The rapid changes in land surface temperatures contributed to the formation of a temperature inversion layer and significant changes in the humidity gradient due to local radiative cooling. In contrast, the temperature on the ocean surface, with its larger specific heat capacity, changed more slowly, and the humidity difference near the sea surface was smaller. The formation of surface ducts over the sea might be more dependent on regional air advection movements, with less influence from local factors, which could explain the lower incidence rate of surface ducts over the sea compared with land. As for elevated ducts, these occurred at relatively high altitudes and were less influenced by the underlying surface. They were mainly caused by weather activities. Therefore, the difference in distribution between the sea and land was not as pronounced as it was for surface ducts. Regarding the latitudinal variations in the incidence rate of ducts within the

Arctic region, the key factors were the changes in the vertical gradients of air temperature and humidity. The closer to the North Pole, the more pronounced the influence of high polar pressure became. Under the influence of prevailing downdrafts throughout the year, the atmospheric stratification near the North Pole remained relatively stable, with minimal changes in the vertical gradients of air temperature and humidity, which thus inhibited the formation of ducts. In contrast, at lower latitudes, the temperature of the underlying surface was higher, and the vertical movement of air was more frequent, which made the occurrence of ducts more likely.

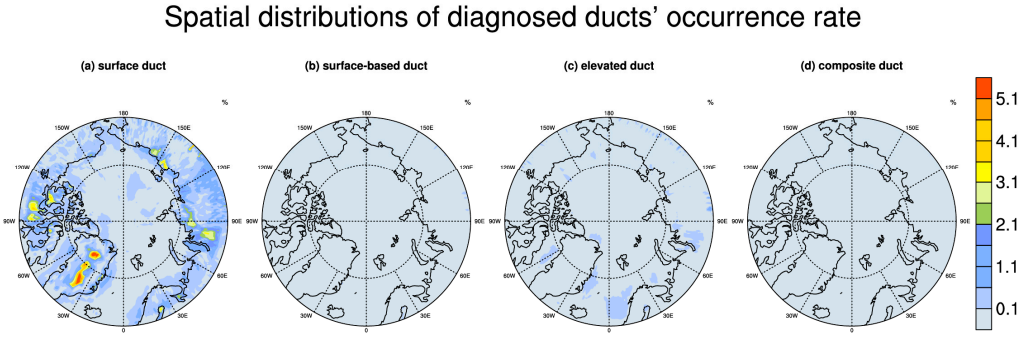

Figure 5. Spatial distributions of the diagnosed occurrence rates for (**a**) simple surface ducts, (**b**) surface-based ducts, (**c**) elevated ducts, and (**d**) composite ducts.

Figure 5b shows the distribution of occurrence rates of surface ducts with a base height. These ducts consisted of an elevated trapping layer superimposed on top of a grounded base layer with a small refractivity gradient, which was typically associated with atmospheric advection activities. Unlike Figure 5a, the occurrence rates for this type of surface duct were very low, with an average rate of 0.0012%, which suggested that surface ducts in the Arctic region were almost entirely simple surface ducts without base heights. For simplicity, both types of surface ducts were analyzed together to examine their variation characteristics.

Similarly, Figure 5c,d illustrate the occurrence rates of single-layer elevated ducts and multilayer composite ducts, respectively. Elevated ducts, characterized by a raised lower boundary, typically form in the lower troposphere below an altitude of 3000 m. They are usually created by an elevated trapping layer positioned above an elevated base layer. As shown in Figure 5c, the average occurrence rate of elevated ducts was 0.016%, mainly concentrated in parts of the Norwegian Sea and Greenland Sea. This distribution might be attributed to the frequent occurrence of sea fog in these regions, where elevated ducts often form within the inversion layer at the fog top. Composite ducts are predominantly associated with intense atmospheric uplift processes, which are exceedingly rare in the Arctic region. As shown in Figure 5d, the occurrence rates of composite duct were nearly zero throughout the five-year simulation period. Consequently, single-layer elevated ducts were used as a representative parameter for all elevated ducts in subsequent analyses. Overall, most ducts were identified on land surrounding the Arctic Ocean and in the Norwegian Sea, which aligned broadly with the findings of Hao et al. [49]. Surface ducts were predominantly observed over land, while elevated ducts were mainly found in the North Atlantic region. The spatial extent of surface ducts was considerably larger than that of elevated ducts, and the occurrence rate of ducts generally decreased with increasing latitude.

Figure 6 illustrates the spatial distribution of three key characteristics—average height, thickness, and strength—for surface and elevated ducts. The average height was calculated as the mean value of the bottom and top heights of the duct layer. To account for topo-

graphic differences between land and sea, all duct heights were adjusted by subtracting the local topographic elevation. Figure 6a depicts the distribution of the average height of surface ducts, with a regional mean of approximately 57.29 m. The highest surface ducts were located around the Norwegian Sea and reached up to 69.08 m, followed by those over much of the Asian continent. Overall, surface duct heights over land were slightly higher than those over the ocean. The height of surface ducts generally decreased with increasing latitude. The spatial distribution of elevated duct heights was closely related to surface temperatures. Influenced by warm ocean currents, the North Atlantic region had warmer and more dynamic sea surface temperatures compared with other regions at similar latitudes, which led to a higher occurrence rate of elevated ducts and their formation at greater altitudes. As shown in Figure 6d, the elevated ducts in the Norwegian Sea region had an average height of 214.83 m, which was much higher than the Arctic-wide average of 150.26 m. The spatial distributions of duct thickness are presented in Figure 6b,e for surface and elevated ducts, respectively. Similar to the average height distribution, the North Atlantic and its coastal areas exhibited the thickest surface and elevated ducts. Figure 6c,f illustrate the distribution of duct strength, which closely aligns with the patterns observed for height and thickness. These observations suggested that elevated ducts occurring at greater heights tended to have thicker and stronger duct layers.

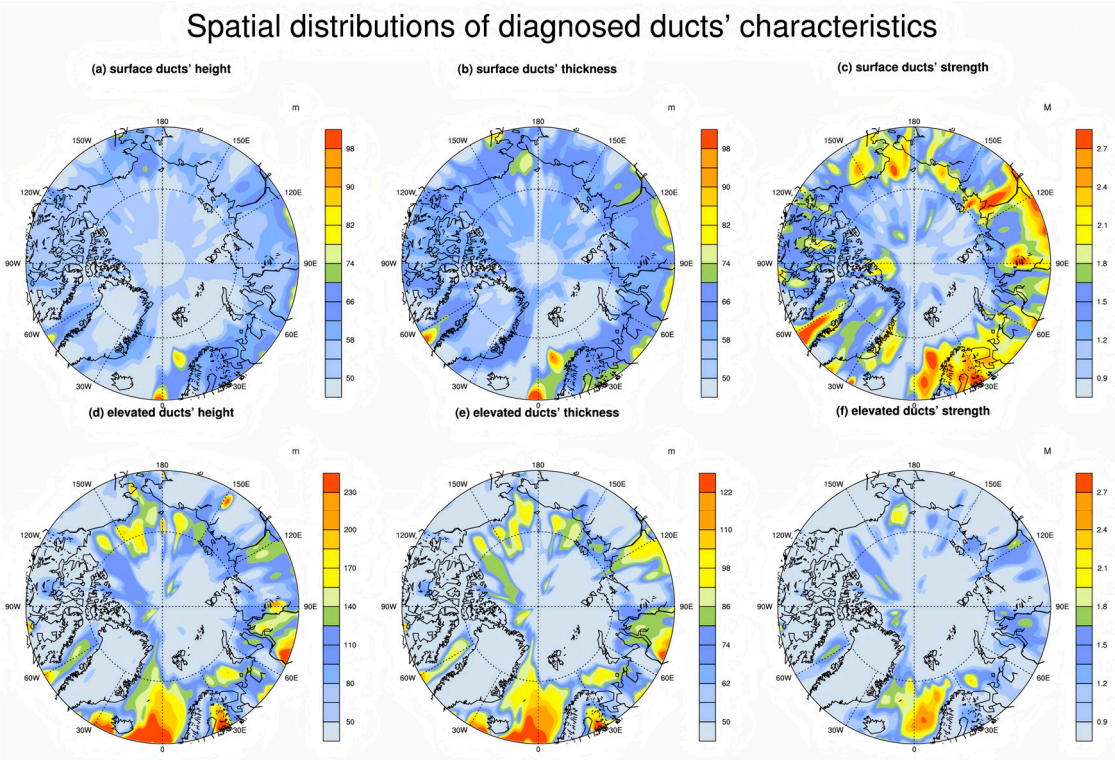

Figure 6. Spatial distributions of the diagnosed duct characteristics: (**a**) surface duct height, (**b**) surface duct thickness, (**c**) surface duct strength, (**d**) elevated duct height, (**e**) elevated duct thickness, and (**f**) elevated duct strength.

Overall, the average height, thickness, and strength of surface ducts were highest in the region near the Norwegian Sea. Outside this area, the surface ducts over land were generally higher and stronger than those over the ocean, with a decreasing trend as increased. In contrast, the distribution of elevated ducts showed no significant differences between land and sea. Several centers of extreme values were observed in the Norwegian Sea across the Asian continent. The strongest elevated ducts occurred in the Norwegian Sea, where the influence of warm currents was most pronounced. In the Arctic region, variations in

atmospheric pressure and temperature driven by latitude differences significantly affected duct occurrence. In the oceanic area north of 75° N, both types of ducts were rarely observed, likely due to the persistent influence of polar high-pressure systems and descending cold air, which inhibited the formation of near-surface temperature inversions that typically promote atmospheric ducting.

4.3. Temporal Variations of the Lower Atmospheric Duct Characteristics

In addition to analyzing the climatological mean state, we examined the seasonal variability of lower atmospheric duct characteristics across different regions. According to the regional distributions of duct occurrence probabilities, three representative areas—Greenland, the Norwegian Sea, and the Kara Sea—were selected to study regional variability. The locations of these three regions are indicated in Figure 3.

Figure 7 presents histograms depicting the monthly variation in occurrence rates for surface and elevated ducts across the three representative regions alongside line plots illustrating the peak monthly occurrence rates.

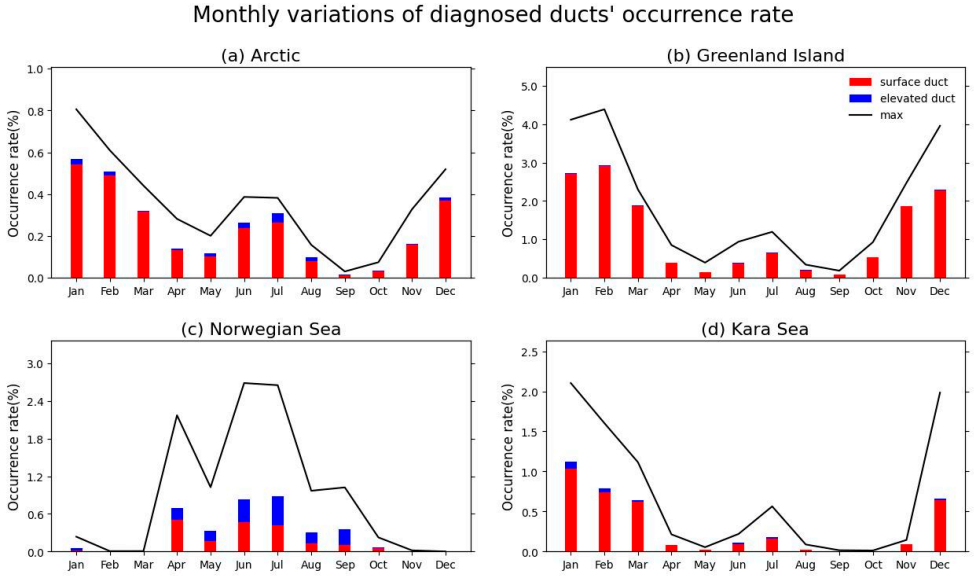

Figure 7. Monthly variation in the diagnosed duct occurrence rates in the (**a**) Arctic, (**b**) Greenland Island, (**c**) Norwegian Sea, and (**d**) Kara Sea. Red bars represent the occurrence rates of surface ducts, blue bars represent the occurrence rates of elevated ducts, and the line indicates the highest monthly occurrence rates.

The monthly rate distributions of surface and elevated ducts for the entire Arctic region (north of 66°34′ N) are shown in Figure 7a. Overall, the occurrence rates of ducts in the Arctic region (Figure 7a) were relatively low, all remaining below 1%, with surface ducts exhibiting a much higher rate than elevated ducts. On average, the highest duct occurrence rates were observed in winter, followed by summer, while autumn had the lowest rates. This seasonal distribution differed significantly from those observed in mid-latitude and low-latitude regions, as revealed by previous studies [24]. Surface ducts accounted for the majority of all ducts, while elevated ducts, which were highly correlated with weather activity, occurred more frequently in summer and winter. The distribution of the highest monthly occurrence rates generally aligned with the average distribution, with the peak rate being over 100% higher than the average. The months with the greatest discrepancy between peak and average probabilities largely corresponded to those with the highest duct occurrence rates. Figure 7b–d display the monthly occurrence rate distributions for the Greenland, Norwegian Sea, and Kara Sea regions, respectively. Compared with the

entire Arctic region (Figure 7a), these three areas had a higher occurrence rate of ducts, although none exceeded 5%. As shown in Figure 5, the Greenland and Kara Sea regions in Figure 7b,d were high-frequency areas for surface ducts, with their seasonal variation being similar to the regional average shown in Figure 7a. In Figure 7c, atmospheric ducts in the Norwegian Sea region were concentrated in the summer, with a very low occurrence rate in the winter. Compared with other regions, in the Norwegian Sea, the occurrence rates of elevated ducts during the summer were significantly higher, which suggested that weather activity in this area was more active. The seasonal distribution of ducts in the Norwegian Sea was similar to the duct characteristics observed in some mid-latitude maritime regions, likely due to the influence of the North Atlantic Drift and higher temperatures in the area. According to multi-year mean distributions of sea surface temperature, the Norwegian Sea region exhibited relatively higher temperatures and a warmer climate, which contributed to the unique duct characteristics in this area. We also examined the duct characteristics in the Bering Strait region. However, owing to the lower sea temperature and weaker influence of warm currents in that area, the seasonal distribution of ducts was more similar to that shown in Figure 7a.

Additionally, Table 1 provides statistics on the CCs between 2 m air temperature (T2m), 2 m relative humidity (RH2m), sea surface temperature (SST), sea level pressure (SLP), and the occurrence rate of ducts. In the Arctic region, surface ducts and elevated ducts exhibited different correlations with these variables. In the Arctic region, surface ducts and elevated ducts exhibited different correlations with these variables. On average, T2m showed the highest correlation with the incidence rate of ducts across the entire region. Specifically, the correlation between the incidence rate of surface ducts and T2m was 0.58, while the correlations between other factors and the incidence rate of ducts did not reach this level. This high correlation suggested that higher air temperatures in the Arctic region were associated with a greater probability of duct occurrence. The CC values in the Arctic region differed from those in mid-latitude areas. In mid-latitude regions, SST typically showed a stronger correlation with surface ducts. In Greenland, the occurrence of surface ducts was closely related to temperature and humidity, with CC values of −0.75 for temperature and −0.57 for humidity. Similarly, in the Kara Sea, surface ducts exhibited a strong negative correlation with both temperature and humidity, with CC values of −0.63 and −0.70, respectively. These findings further confirmed that in cold polar environments, a drop in temperature and humidity was a key factor for duct formation. In contrast, surface ducts in the Norwegian Sea displayed a positive correlation with various variables, which indicated that warmer conditions promoted the formation of more surface ducts. Higher temperature, humidity, sea surface temperature, and sea surface pressure all contributed to this trend. In this region, duct formation was most strongly influenced by changes in pressure.

Table 1. CCs between the occurrence rate of ducts and surface meteorological elements.

Duct Occurrence Rate	CC with T2m		CC with RH2m		CC with SST		CC with SLP	
	Surface Duct	Elevated Duct	Surface Duct	Elevated Duct	Surface Duct	Elevated Duct	Surface Duct	Elevated Duct
Arctic	0.58	0.27	0.21	−0.02	−0.18	0.02	0.31	−0.10
Greenland Island	−0.75	0.38	−0.57	0.34	−0.41	0.17	−0.67	0.06
Norwegian sea	0.31	0.41	0.36	0.45	0.15	0.30	0.49	0.50
Kara sea	−0.63	−0.37	−0.70	−0.42	−0.37	−0.22	−0.08	0.17

Figure 8 shows the monthly mean height, thickness, and strength of surface and elevated ducts in the Arctic region (north of the Arctic Circle) and three typical areas. Data for certain months are missing in some regions due to the absence of duct phenomena. Figure 8a,d,g,j display the duct heights for the Arctic regional averages and the three typical

areas. During the warmer summer months, when air movement was more active, ducts tended to form at higher altitudes. Surface duct heights were generally around 70 m, while elevated duct heights were around 360 m, both of which were lower compared with duct heights in mid-latitude regions. Surface duct height did not vary significantly throughout the year, with an average height of 56.47 m in the Arctic region (Figure 8a). The average heights in the Greenland (Figure 8d), Norwegian Sea (Figure 8g), and Kara Sea (Figure 8j) regions were 53.30 m, 64.00 m, and 56.28 m, respectively.

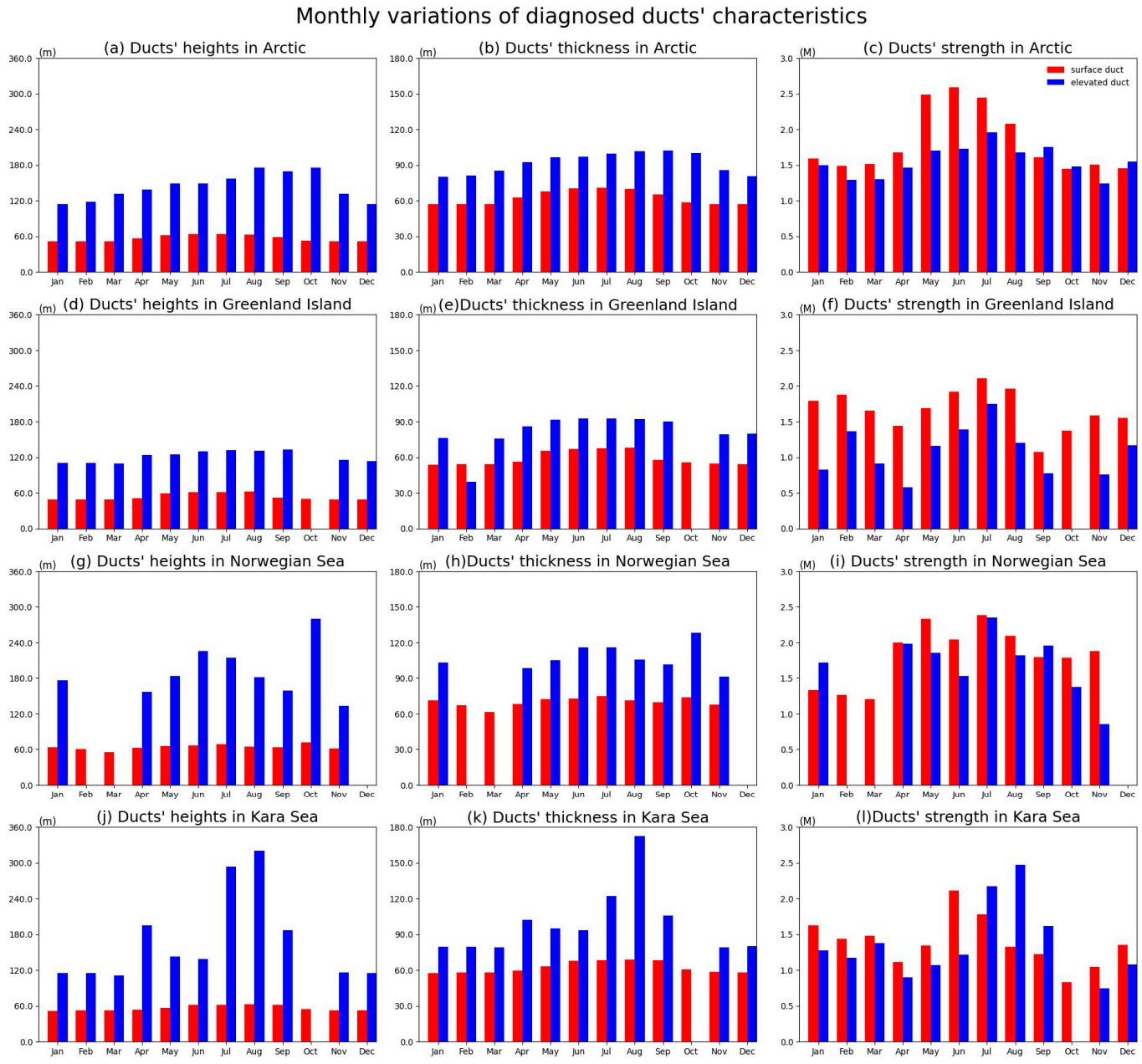

Figure 8. Monthly variations of the diagnosed duct characteristics, including (**a**) heights, (**b**) thickness, and (**c**) strength in the Arctic; (**d**) heights, (**e**) thickness, and (**f**) strength in Greenland Island; the ducts' (**g**) heights, (**h**) thickness, and (**i**) strength in the Norwegian Sea; and the ducts' (**j**) heights, (**k**) thickness and (**l**) strength in the Kara Sea. The red columns represent surface duct characteristics, and the blue columns represent elevated duct characteristics.

Elevated duct heights were generally higher than surface duct heights, with an average of 143.40 m for the entire Arctic region (Figure 8a). The average heights for the Greenland

(Figure 8d), Norwegian Sea (Figure 8g), and Kara Sea (Figure 8j) regions were 121.17 m, 191.11 m, and 167.90 m, respectively. Seasonal differences in duct heights were not significant for the entire Arctic region (Figure 8a) or in Greenland (Figure 8d), but they were more pronounced in the Norwegian Sea (Figure 8g) or Kara Sea (Figure 8j). In these areas, duct heights were higher in the summer, which indicated more intense weather activity during the warmer months. Unlike the relatively consistent distribution throughout the year in the Norwegian Sea region (Figure 8g), duct heights in the Kara Sea region (Figure 8j) were significantly higher in July and August compared with other months and reached levels similar to Greenland's duct heights (Figure 8d) during the winter. This distribution corresponded with the temperature and weather activity of the region, with the peak duct heights coinciding with the highest temperatures and periods of increased precipitation.

Figure 8b,e,h,k show the monthly distribution of duct thickness. The seasonal variations in duct thickness were generally consistent with those of duct height, with the greatest thickness typically occurring in the summer and autumn when duct heights were at their highest. Surface ducts generally had smaller thicknesses than elevated ducts, and their seasonal variation was less pronounced compared with elevated ducts. In the entire Arctic region (Figure 8b), the average thickness of surface ducts was 62.56 m, while elevated ducts had an average thickness of 91.83, which was roughly consistent with the seasonal variation in duct thickness reported by Qin et al. [15], according to the data from 1989 to 2018. The variation in duct thickness throughout the year in the Greenland region (Figure 8e) was similarly insignificant, with an average surface duct thickness of 59.00 m and an average elevated duct thickness of 81.34 m. In the Norwegian Sea region (Figure 8h), ducts were thicker than in other areas, with an average surface duct thickness of 69.98 m and an elevated duct thickness of 107.19 m, which showed relatively higher thickness in June and July. In the Kara Sea region (Figure 8k), the average thickness of surface ducts was 62.25 m, and elevated ducts had an average thickness of 98.86 m. The seasonal variation in elevated duct thickness was quite pronounced, with maximum thickness observed in July and August.

Figure 8c,f,i,l show the monthly distribution of duct strength. Overall, the strength of surface ducts was slightly higher than that of elevated ducts. The average strength of surface ducts in the entire Arctic region (Figure 8c) was 1.82 M, while the average strength for elevated ducts was 1.55 M. The maximum strength for both types of ducts typically occurred in summer, consistent with the seasonal variations in height and thickness. In Greenland (Figure 8f), the strength difference between surface and elevated ducts was more pronounced than the regional average, with surface ducts having an average strength of 1.67 M, while elevated ducts had an average strength of only 1.08 M. In the Norwegian Sea region (Figure 8i), the strength difference between the two types of ducts was smaller, with the average strength of surface ducts at 1.83 M and elevated ducts at 1.71 M. In the Kara Sea region (Figure 8l), the average strength of surface ducts was 1.39 M, while elevated ducts had an average strength of 1.37 M. Strength values showed a significant increase during the summer, which corresponded to the seasonal variations in height and thickness. The peak strength of surface ducts occurred in June and July, slightly earlier than that of elevated ducts, which peaked in July and August.

Overall, there were significant seasonal variations and regional differences in duct height, thickness, and strength across the Arctic region. Elevated ducts were generally taller and thicker than surface ducts, but their average strength was lower. This suggests that it was more challenging to form strong ducts at higher altitudes in cold polar regions. Both types of ducts typically reach their maximum height, thickness, and strength in the summer, with these characteristics being relatively weaker in the autumn and winter. This pattern did not align with the seasonal distribution of duct occurrence rate. That is, although the

duct occurrence in the Arctic region was higher in winter than in summer, the characteristic values—such as height, thickness, and strength—were lower in winter compared with summer. The three typical regions of Greenland, the Norwegian Sea, and the Kara Sea exhibited significant differences in duct characteristics. The warmer Norwegian Sea region was particularly unique, which showed seasonal variations more similar to those in mid-latitude regions. In the Norwegian Sea, both the occurrence rate and characteristics of ducts followed consistent seasonal patterns, with maxima typically occurring in the summer. In contrast, the ducts in Greenland and the Kara Sea displayed seasonal changes similar to the Arctic region's average. The main difference was that the duct characteristics in the Kara Sea were more pronounced during the summer, influenced by local climate effects.

Figure 9 shows the time series of the occurrence rates for surface and elevated ducts during the simulation period. To explore the relationship between the polar vortex and atmospheric ducts, Figure 9 also includes the time series of the PVI and PVA indices, calculated using the method described in Section 2.3. In the entire Arctic region (Figure 9a), the duct occurrence rate displayed a clear seasonal cycle, along with a slight decreasing trend over the years. Surface ducts accounted for the majority of the total duct occurrence rate, while the proportion of elevated ducts remained relatively low. The CCs between the surface duct occurrence rate and the PVA and PVI indices were also calculated. These coefficients were relatively low and indicated no significant correlations between the occurrence of ducts and the development of the polar vortex. The polar vortex was mainly associated with large-scale cold air outbreaks and changes in polar atmospheric circulation. However, as shown in the figure, the changes in PVI and PVA did not lead to a noticeable increase or decrease in the occurrence of ducts.

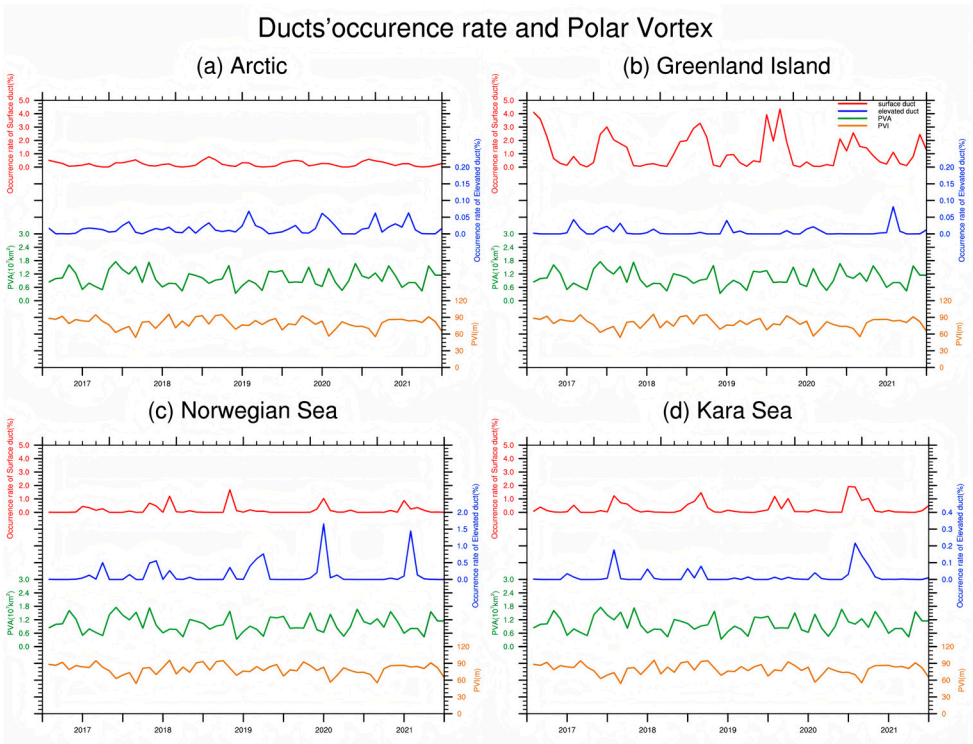

Figure 9. Monthly series of duct occurrence rates and polar vortex indices (PVI and PVA), including the series for (**a**) the Arctic, (**b**) Greenland Island, (**c**) the Norwegian Sea, and (**d**) the Kara Sea. The red and blue lines represent the occurrence rate series for surface ducts and elevated ducts, respectively. The green and brown lines represent the PVA and PVI indices, which are the same across all four subfigures.

The ducts in the three typical regions (Figure 9b–d) exhibited different temporal variations and responses to polar vortex activity. In the Greenland region (Figure 9b), there was a slight decreasing trend in duct occurrence, with the total duct rate decreasing from 1.50% in 2017 to 1.09% in 2021. The CCs between surface duct occurrence and PVA and PVI in this region were 0.21 and −0.04, respectively. For elevated ducts, the CCs were −0.05 and −0.13.

The total duct occurrence rate in the Norwegian Sea region (Figure 9c) showed an increasing trend and rose from 0.16% in 2017 to 0.36% in 2019. There was a slight decrease in 2020 and 2021, but the rate remained around 0.30%. Most of this increase was due to the growth of elevated ducts (blue line). The CCs between surface duct occurrence and PVA and PVI were −0.05 and 0.17, respectively. For elevated ducts, the CCs were −0.20 and 0.06, respectively.

The Kara Sea region (Figure 9d) also showed an increasing trend in duct occurrence rate and rose from 0.12% in 2017 to 0.43% in 2021. This increase was mainly due to the growth of surface ducts. According to Table 1 and the time series of surface meteorological elements, this trend was likely related to global climate warming and accelerated sea ice melting in the Kara Sea. The warming effect and transition from ice to water likely altered the air temperature and humidity gradient near the sea surface, which may have facilitated the formation of ducts. The CCs between duct occurrence and PVA and PVI were still relatively low, with values of 0.03 and −0.15 for surface ducts, and 0.03 and −0.23 for elevated ducts.

The time series of duct height, thickness, and strength in the typical regions did not exhibit clear trends during the simulation period, so they were not displayed. However, Table 2 lists the CCs between the series of duct height, thickness, and strength in each region and the PVI and PVA indices. As shown in the table, although PVI and PVA had a low correlation with duct occurrence rates, these two indices showed a strong correlation with certain duct characteristic parameters. Overall, in the Arctic region, the negative correlation of PVA with duct characteristics was stronger than that of PVI, with some coefficients approaching 0.5. This correlation suggested that an expansion of the polar vortex area often led to a reduction in duct height, thickness, and strength, while changes in the strength of the polar vortex had minimal impact on duct characteristics. Furthermore, PVA showed a stronger correlation with surface ducts, while its effect on higher-altitude elevated ducts was weaker. Among the three typical regions, Greenland was notably influenced by polar vortex activity, with CCs aligning with the Arctic regional averages. In contrast, the CCs in the Norwegian Sea and Kara Sea regions were comparatively weak. Particularly in the Kara Sea region, the correlations between PVA and PVI with duct parameters were nearly zero, which indicated that variations in the polar vortex were not a key factor influencing duct characteristics in that area.

Table 2. CCs of the duct characteristics with the polar vortex indices.

	CC with PVA			CC with PVI			CC with PVA			CC with PVI		
	Surface Duct Height	Surface Duct Thickness	Surface Duct Strength	Surface Duct Height	Surface Duct Thickness	Surface Duct Strength	Elevated Duct Height	Elevated Duct Thickness	Elevated Duct Strength	Elevated Duct Height	Elevated Duct Thickness	Elevated Duct Strength
Arctic	−0.26	−0.43	−0.34	0.15	0.04	0.01	0.26	0.30	0.21	0.15	0.15	0.02
Greenland Island	−0.42	−0.42	0.01	0.04	0.04	0.04	−0.13	−0.13	−0.13	−0.10	−0.10	−0.10
Norwegian Sea	−0.21	−0.21	−0.21	0.05	0.05	0.05	−0.27	−0.27	−0.26	0.12	0.14	0.15
Kara Sea	0.01	0.01	0.02	−0.10	−0.10	−0.10	−0.05	−0.05	−0.04	−0.22	−0.22	−0.23

5. Conclusions and Discussion

In summary, the key conclusions of this study are as follows.

(1) The newly developed duct diagnostic model demonstrated excellent performance. Compared with sounding data from Ostrov Dikson, Barrow, and Danmarkshavn, the mean errors of the simulated modified atmospheric refractivity ranged from −1 M to 3 M, with RMSEs between 0 and 5 M. The overall simulation error level was slightly lower than that of the ERA5 reanalysis data, and the simulation errors decreased gradually with increasing height. The simulation results also showed a high correlation with the observations, with an average correlation coefficient greater than 0.81, which accurately reflected the temporal variability of the modified refractivity.

(2) The average occurrence rate of ducts in the Arctic region was 0.25%, much lower than in lower-latitude regions. Among the various types of lower atmospheric ducts, only simple surface ducts and elevated ducts were commonly observed in the Arctic. Surface-based and composite ducts were rarely detected during the simulation period. The occurrence rate of surface ducts (including both simple surface ducts and surface-based ducts) was 0.23%, much higher than the 0.016% for elevated ducts. High occurrence areas were mainly found in Greenland Island and continental regions of the Arctic. The occurrence rate of surface ducts on land was notably higher than that over the ocean. Elevated ducts occurred more frequently over ocean areas, with higher occurrence rates in the Norwegian Sea and the waters near Greenland. Most ducts in the region were detected south of 75° N, and as latitude increased, the occurrence rates of surface ducts gradually decreased.

(3) The duct height, thickness, and strength varied consistently. In areas with higher duct height, the thickness and strength were typically higher as well. However, the spatial distribution of surface duct height, thickness, and strength did not align with the distribution of occurrence rates. The average height, thickness, and strength of surface ducts were higher in the North Atlantic and Asian continent. In contrast to surface ducts, the height, thickness, and strength of elevated ducts were more closely related to their occurrence rates. In the North Atlantic, the characteristic parameters of elevated ducts were significantly stronger compared with those of other regions.

(4) The seasonal variation of atmospheric ducts in the Arctic was highly pronounced. The occurrence rate of ducts was highest in winter, followed by summer, with the lowest rates in autumn. Most of the ducts were surface ducts, while elevated ducts mainly occurred in summer and winter. In different regions, the seasonal variation of ducts exhibited distinct characteristics. The occurrence rate of ducts in Greenland, the Norwegian Sea, and the Kara Sea was higher than the Arctic average. In Greenland and the Kara Sea, ducts occurred most frequently in winter and less often in summer. In contrast, in the Norwegian Sea, most ducts appeared in summer, with the highest rate of elevated ducts in the entire Arctic region. The interannual variability in the Norwegian Sea was also the most pronounced, resulting in a significant difference between the maximum and average duct occurrence rates. Regarding the correlation between surface meteorological factors and duct formation, temperature and humidity were closely related to duct occurrence. Surface ducts, in most areas, showed a clear correlation with temperature and humidity changes, while elevated ducts had a weaker correlation.

(5) Seasonal differences in the duct strength were more pronounced than those in duct height and thickness. In the Arctic, surface ducts had lower values for both duct height and thickness compared with elevated ducts, but the strength of surface ducts was slightly greater than that of elevated ducts. Although ducts did not occur most frequently in summer, their characteristic parameters typically reached their maximum during this season. Compared with Greenland, the Norwegian Sea and the Kara

Sea region showed more pronounced seasonal differences in duct occurrence, which aligned with the seasonal changes in temperature and precipitation in these areas.

(6) In terms of interannual variability, the average duct occurrence rate in the Arctic region and Greenland showed a slight decreasing trend. However, the duct occurrence rate in the Norwegian Sea and the Kara Sea, influenced by the North Atlantic warm current, exhibited an increasing trend each year. Regarding the interannual variability of duct characteristic parameters, no clear trends of annual increase or decrease were observed.

(7) In the Arctic region, no significant correlation was found between the polar vortex indices and the occurrence rate of atmospheric ducts. However, a clear negative correlation existed between the polar vortex indices and the duct characteristic parameters. Furthermore, the area of the polar vortex had a greater impact on the duct characteristics than the intensity of the polar vortex. The correlation between the polar vortex and surface duct parameters was stronger, while its influence on higher-altitude elevated ducts was comparatively weaker. Regionally, the Greenland area was notably influenced by polar vortex activity, whereas the Norwegian Sea and Kara Sea regions experienced less influence.

In this study, a diagnostic model for lower atmospheric ducts was developed using the Polar WRF model. A dynamical downscaling simulation was then conducted to investigate the spatial and temporal characteristics of lower atmospheric ducts in the Arctic. The simulation results were evaluated against observations from three radiosonde stations: Ostrov Dikson, Barrow, and Danmarkshavn. Subsequently, the temporal and spatial variability of duct characteristics in the Arctic was analyzed based on duct diagnostics.

There are still some uncertainties in the results of this study, and further improvements in model development, experimental design, and analysis are needed in the future. Specifically, these include the following:

(1) Regarding model development, using the same parameterization scheme across the vast Arctic region in a mesoscale weather model likely contributed to varying error levels in different areas. Previous studies with climate models have employed different parameterization schemes for different regions. Future simulations should follow a similar approach to enhance the local accuracy of PWRF. Additionally, the PWRF model did not account for dynamic feedback processes from the ocean surface, which limited its ability to capture the ocean's influence when studying the relationship between atmospheric ducts and climate change. To address this, future simulations should incorporate a coupled atmosphere-ocean model, which would yield more objective and comprehensive results.

(2) Regarding experimental design, this study conducted simulations over a five-year period, which was insufficient for long-term climate studies. As a result, the findings may not fully capture interannual variability. Future studies should extend the simulation period to obtain more representative climate characteristics. During the simulation period of this study, the sample size for different duct types was limited. Consequently, we only analyzed the overall characteristics of surface and elevated ducts. In future research, longer-term data should be used to conduct a more detailed evaluation of the characteristics of various duct types.

(3) In evaluating the simulation results, this study selected three radiosonde stations in different locations for model validation. The study focused mainly on the modified atmospheric refractivity index. In addition, the RMSEs for air temperature and humidity were also assessed. The RMSE for temperature at the Ostrov Dikson station was 1.96 K, while at the Barrow and Danmarkshavn stations, it was 1.12 K and 2.15 K, respectively. The RMSE for relative humidity at Ostrov Dikson was 5.59%, while at

Barrow and Danmarkshavn, it was 5.39% and 5.36%, respectively. The simulated temperature and humidity errors remained relatively low, which indicated that the PWRF model performed well in simulating polar weather. However, due to the limited number of validation stations, some randomness still influenced the evaluation results. Additionally, the sounding observations provided data only at two time points each day. In the future, more stations and a denser observation dataset will be necessary for a more thorough evaluation of the model's performance.

(4) In the analysis, owing to space limitations constraints, this study provided only a basic overview of the temporal and spatial characteristics of lower atmospheric ducts. Future efforts will focus more on exploring the relationship between duct characteristics and changes in sea ice and ocean surfaces. Additionally, while few studies have used dynamical downscaling to simulate atmospheric ducts in polar regions, some studies have directly diagnosed reanalysis data to obtain duct information. However, these studies face challenges due to the limited number of vertical levels in reanalysis data, which makes it difficult to capture atmospheric duct information by directly diagnosing the vertical variation of atmospheric refractivity. To address this, some researchers have processed the reanalysis data further. For example, they have employed various methods such as spline interpolation to identify additional inflection points in the vertical distributions [50]. In this study, we used only linear interpolation during the diagnostic process, which resulted in very few new inflection points. As a result, some discrepancies were observed in the duct diagnostic results compared with previous studies. Specifically, the rates of duct occurrence in this study were lower than those reported by Qin et al. [22], who used ERA5 data from 1989 to 2018. To explore this difference, we selected ERA5 data from Ostrov Dikson, Barrow, and Danmarkshavn stations over five years for a direct duct diagnosis. However, this method was almost unable to detect any ducts. Since Qin et al. did not reveal the specifics of their diagnostic process, the differences between their results and ours are likely due to the duct diagnostic schemes, particularly in how the modified atmospheric refractivity data was processed. This study mainly used a numerical model to dynamically downscale the coarser vertical resolution of reanalysis data. In contrast, the method of directly diagnosing reanalysis data often involved applying other mathematical techniques to increase the vertical resolution before diagnosing the ducts. This difference in diagnostic methods resulted in variations in the final duct characteristics. Moving forward, we will continue to monitor developments in this area and further improve our algorithms and models.

Author Contributions: Writing—review and editing, J.Z. and M.S.; methodology, X.Z.; software, P.Y.; validation, Z.Q. and S.Y.; resources, B.W.; supervision, Z.L.; conceptualization, T.H.; writing—original draft preparation, J.W. All authors have read and agreed to the published version of the manuscript.

Funding: This study was financially supported by the National Key Research and Development Program of China (2022YFC3104202), the National Natural Science Foundation of China (Grant nos. 42076195, 42206188, 42176185), the Natural Science Foundation of Shandong province, China (ZR2022MD100, ZR2021MD114), the Key R&D Plan of Shandong Province, China (2023CXPT015), the "Four Projects" of computer science (2021JC02002) and the basic research foundation (2024GH05, 2023PY004, 2023JBZ02, 2023JBZ01, and 2023PY050) in Qilu University of Technology.

Institutional Review Board Statement: Not applicable.

Informed Consent Statement: Not applicable.

Data Availability Statement: The data are not publicly available due to internal policy of Qilu University of Technology.

Conflicts of Interest: The authors declare no conflicts of interest.

References

1. Hao, X.; Li, Q.; Guo, L.; Lin, L.; Ding, Z.; Zhao, Z.; Yi, W. Digital Maps of Atmospheric Refractivity and Atmospheric Ducts Based on a Meteorological Observation Datasets. *IEEE Trans. Antennas Propag.* **2022**, *70*, 2873–2883. [CrossRef]
2. Yang, C.; Wang, J. The Investigation of Cooperation Diversity for Communication Exploiting Evaporation Ducts in the South China Sea. *IEEE Trans. Antennas Propag.* **2022**, *70*, 8337–8347. [CrossRef]
3. Wang, S.; Yang, K.; Shi, Y.; Zhang, H.; Yang, F.; Hu, D.; Dong, G.; Shu, Y. Long-Term over-the-Horizon Microwave Channel Measurements and Statistical Analysis in Evaporation Ducts over the Yellow Sea. *Front. Mar. Sci.* **2023**, *10*, 1077470. [CrossRef]
4. Zhou, T.; Sun, T.; Hu, H.; Xu, H.; Yang, Y.; Harjula, I.; Koucheryavy, Y. Analysis and Prediction of 100 Km–Scale Atmospheric Duct Interference in TD–LTE Networks. *J. Commun. Inf. Netw.* **2017**, *2*, 66–80. [CrossRef]
5. Yao, Z.; Zhao, B.; Li, W.; Zhu, Y.; Du, J.; Dai, F.S. Analysis on characteristics of atmospheric duct and its effects on the propagation of electromagnetic wave. *J. Meteorol. Res.* **2001**, *15*, 233–248.
6. Liu, F.; Pan, J.; Zhou, X.; Li, G.Y. Atmospheric Ducting Effect in Wireless Communications: Challenges and Opportunities. *J. Commun. Inf. Netw.* **2021**, *6*, 101–109. [CrossRef]
7. Huang, L.; Liu, C.; Wang, H.; Zhu, Q.; Zhang, L.; Han, J.; Zhang, Y.; Wang, Q. Experimental analysis of atmospheric ducts and navigation radar over-the-horizon detection. *Remote Sens.* **2022**, *14*, 2588. [CrossRef]
8. Yang, N.; Su, D.; Wang, T. Atmospheric Ducts and Their Electromagnetic Propagation Characteristics in the Northwestern South China Sea. *Remote Sens.* **2023**, *15*, 3317. [CrossRef]
9. Ma, J.; Wang, J.; Yang, C. Long-Range Microwave Links Guided by Evaporation Ducts. *IEEE Commun. Mag.* **2022**, *60*, 68–72. [CrossRef]
10. Shi, Y.; Wang, S.; Yang, F.; Yang, K. Statistical analysis of hybrid atmospheric ducts over the Northern South China sea and their influence on over–the–horizon electromagnetic wave propagation. *J. Mar. Sci. Eng.* **2023**, *11*, 669. [CrossRef]
11. Norin, L.; Wellander, N.; Devasthale, A. Anomalous propagation and the sinking of the Russian warship Moskva. *Bull. Am. Meteorol. Soc.* **2023**, *104*, 2286–2304. [CrossRef]
12. Sirkova, I. Brief review on PE method application to propagation channel modeling in sea environment. *Open Eng.* **2012**, *2*, 19–38. [CrossRef]
13. Turton, J.D.; Bennetts, D.A.; Farmer, S.G. An introduction to radio ducting. *Meteorol. Mag.* **1988**, *117*, 245–254.
14. Bean, B.R.; Dutton, E.J. *Radio Meteorology*; Government Printing Office: Washington, DC, USA, 1966.
15. Sirkova, I. Duct Occurrence and Characteristics for Bulgarian Black Sea Shore Derived from ECMWF Data. *J. Atmos. Sol.–Terr. Phys.* **2015**, *135*, 107–117. [CrossRef]
16. Zhu, M.; Atkinson, B.W. Simulated climatology of atmospheric ducts over the Persian Gulf. *Bound. Layer Meteorol.* **2005**, *115*, 433–452. [CrossRef]
17. Atkinson, B.W.; Zhu, M. Coastal effects on radar propagation in atmospheric ducting conditions. *Meteorol. Appl.* **2006**, *13*, 53–62. [CrossRef]
18. Burk, S.D.; Thompson, W.T. Mesoscale modeling of summertime refractive conditions in the Southern California Bight. *J. Appl. Meteorol.* **1997**, *36*, 22–31. [CrossRef]
19. Haack, T.; Burk, S.D. Summertime marine refractivity conditions along coastal California. *J. Appl. Meteorol. Climatol.* **2001**, *40*, 673–687. [CrossRef]
20. Overland, J.; Dunlea, E.; Box, J.E.; Corell, R.; Forsius, M.; Kattsov, V.; Olsen, M.S.; Pawlak, J.; Reiersen, L.O.; Wang, M. The urgency of Arctic change. *Polar Sci.* **2019**, *21*, 6–13. [CrossRef]
21. Kwok, R. Arctic Sea ice thickness, volume, and multiyear ice coverage: Losses and coupled variability (1958–2018). *Environ. Res. Lett.* **2018**, *13*, 105005. [CrossRef]
22. Qin, T.; Su, B.; Chen, L.; Yang, J.; Sun, H.; Ma, J.; Yu, W. Arctic Atmospheric Ducting Characteristics and Their Connections with Arctic Oscillation and Sea Ice. *Atmosphere* **2022**, *13*, 2119. [CrossRef]
23. Zhu, J.; Zou, H.; Kong, L.; Zhou, L.; Li, P.; Cheng, W.; Bian, S. Surface atmospheric duct over Svalbard, Arctic, related to atmospheric and ocean conditions in winter. *Arct. Antarct. Alp. Res.* **2022**, *54*, 264–273. [CrossRef]
24. Liu, Q.; Zhao, X.; Zou, J.; Hu, T.; Qiu, Z.; Wang, B.; Li, Z.; Cui, C.; Cao, R. Investigating the spatio–temporal characteristics of lower atmospheric ducts across the China seas by performing a long–term simulation using the WRF model. *Front. Mar. Sci.* **2024**, *11*, 1332805. [CrossRef]
25. Liu, Q.; Zhao, X.; Zou, J.; Li, Y.; Qiu, Z.; Hu, T.; Wang, B.; Li, Z. Development of a Numerical Prediction Model for Marine Lower Atmospheric Ducts and Its Evaluation across the South China Sea. *J. Mar. Sci. Eng.* **2024**, *12*, 141. [CrossRef]
26. Hines, K.M.; Bromwich, D.H.; Bai, L.S.; Barlage, M.; Slater, A.G. Development and testing of Polar WRF. Part III: Arctic land. *J. Clim.* **2011**, *24*, 26–48. [CrossRef]

27. Deb, P.; Orr, A.; Hosking, J.S.; Phillips, T.; Turner, J.; Bannister, D.; Pope, J.O.; Colwell, S. An assessment of the Polar Weather Research and Forecasting (WRF) model representation of near-surface meteorological variables over West Antarctica. *J. Geophys. Res.* **2016**, *121*, 1532–1548. [CrossRef]
28. Wilson, A.B.; Bromwich, D.H.; Hines, K.M. Evaluation of Polar WRF forecasts on the Arctic System Reanalysis domain: Surface and upper air analysis. *J. Geophys. Res.* **2011**, *116*, D11112. [CrossRef]
29. Wilson, A.B.; Bromwich, D.H.; Hines, K.M. Evaluation of Polar WRF forecasts on the Arctic System Reanalysis domain: 2. Atmospheric Hydrologic Cycle. *J. Geophys. Res.* **2012**, *117*, D04107. [CrossRef]
30. Hines, K.M.; Bromwich, D.H. Development and testing of Polar Weather Research and Forecasting (WRF) model. Part I: Greenland ice sheet meteorology. *Mon. Weather Rev.* **2008**, *136*, 1971–1989. [CrossRef]
31. Bromwich, D.H.; Hines, K.M.; Bai, L.S. Development and testing of polar weather research and forecasting model: 2. Arctic Ocean. *J. Geophys. Res.* **2009**, *114*, D08112. [CrossRef]
32. Xu, L.; Yardim, C.; Mukherjee, S.; Burkholder, R.J.; Wang, Q. Frequency Diversity in Electromagnetic Remote Sensing of Lower Atmospheric Refractivity. *IEEE Trans. Antennas Propag.* **2022**, *70*, 547–555. [CrossRef]
33. Cheng, Y.; Zhou, S.; Wang, D.; Lu, Y.; Huang, K.; Yao, J.; You, X. Observed characteristics of atmospheric ducts over the South China Sea in autumn. *Chin. J. Oceanol. Limnol.* **2016**, *34*, 619–628. [CrossRef]
34. Hitney, H.; Vieth, R. Statistical assessment of evaporation duct propagation. *IEEE Trans. Antennas Propag.* **1990**, *38*, 794–799. [CrossRef]
35. Burnett, A.W. Size variations and long-wave circulation within the January Northern Hemisphere circumpolar vortex: 1946–1989. *J. Clim.* **1993**, *6*, 1914–1920. [CrossRef]
36. Davis, R.; Benkovic, S. Climatological variations in the Northern Hemisphere circumpolar vortex in January. *Theor. Appl. Climatol.* **1992**, *46*, 63–73. [CrossRef]
37. Markham, C.G. A quick and direct method for estimating mean monthly global temperatures from 500mb data. *Prof. Geogr.* **1985**, *37*, 72–74. [CrossRef]
38. Kolstad, E.W.; Breiteig, T.; Scaife, A.A. The association between stratospheric weak polar vortex events and cold air outbreaks in the Northern Hemisphere. *Q. J. R. Meteorol. Soc.* **2010**, *136*, 886–893. [CrossRef]
39. Peterlin, A.; Scheeringa, K.L. Digital circumpolar vortex area index calculations for the northern and southern hemispheres. *Natl. Weather Dig.* **2004**, *128*, 43–46.
40. Hersbach, H.; Bell, B.; Berrisford, P.; Hirahara, S. The ERA5 Global Reanalysis. *Q. J. R. Meteorol. Soc.* **2020**, *146*, 1999–2049. [CrossRef]
41. Hong, S.Y.; Lim, J.O. The WRF single–moment 6–class microphysics scheme (WSM6). *Asia–Pac. J. Atmos. Sci.* **2006**, *42*, 129–151.
42. Beljaars, A.C. The parametrization of surface fluxes in large-scale models under free convection. *Q. J. R. Meteorol. Soc.* **1995**, *121*, 255–270.
43. Bae, S.Y.; Hong, S.Y.; Tao, W.K. Development of a single–moment cloud microphysics scheme with prognostic hail for the Weather Research and Forecasting (WRF) model. *Asia–Pac. J. Atmos. Sci.* **2019**, *55*, 233–245. [CrossRef]
44. Mlawer, E.J.; Taubman, S.J.; Brown, P.D.; Iacono, M.J.; Clough, S.A. Radiative transfer for inhomogeneous atmospheres: RRTM, a validated correlated-k model for the longwave. *J. Geophys. Res.* **1997**, *102*, 16663–16682. [CrossRef]
45. Dudhia, J. Numerical study of convection observed during the winter monsoon experiment using a mesoscale two–dimensional model. *J. Atmos. Sci.* **1989**, *46*, 3077–3107. [CrossRef]
46. Grell, G.A.; Freitas, S.R. A scale and aerosol aware stochastic convective parameterization for weather and air quality modeling. *Atmos. Chem. Phys.* **2014**, *14*, 5233–5250. [CrossRef]
47. Stauffer, D.R.; Seaman, N.L. Use of four-dimensional data assimilation in a limited-area mesoscale model. Part I: Experiments with synoptic-scale data. *Mon. Weather Rev.* **1990**, *118*, 1250–1277. [CrossRef]
48. Lo, J.C.F.; Yang, Z.L.; Pielke Sr, R.A. Assessment of three dynamical climate downscaling methods using the Weather Research and Forecasting (WRF) model. *J. Geophys. Res.* **2008**, *113*, D09112. [CrossRef]
49. Hao, X.; Li, Q.; Guo, L. Spatial and temporal characteristics of the atmosphere ducts over the North Pole. *Chin. J. Polar Res.* **2018**, *30*, 349–359.
50. Zhou, L.; Zheng, G.; Li, X.; Yang, J.; Ren, L.; Chen, P.; Zhang, H.; Lou, X. An improved local gradient method for sea surface wind direction retrieval from SAR imagery. *Remote Sens.* **2017**, *9*, 671. [CrossRef]